

SUPPORTING INFORMATION for DT-ART-06-2015-002403

Dinuclear Iridium and Rhodium Complexes with Bridging
Arylimidazolide- N^3,C^2 Ligands: Synthetic, Structural,
Reactivity, Electrochemical and Spectroscopic Studies

Fan He,^a Laurent Ruhlmann,^b Jean-Paul Gisselbrecht,^b Sylvie Choua,^c Maylis Orio,^e Marcel Wesolek,^a Andreas A. Danopoulos,^{*a,d} Pierre Braunstein^{*a}

^a Laboratoire de Chimie de Coordination, Institut de Chimie (UMR 7177 CNRS), Université de Strasbourg, 4 rue Blaise Pascal, 67081 Strasbourg Cedex (France)

^b Laboratoire d'Electrochimie et de Chimie Physique du Corps Solide, Institut de Chimie (UMR 7177 CNRS), Université de Strasbourg, 4 rue Blaise Pascal, 67081 Strasbourg Cedex (France)

^c Institut de Chimie, Université de Strasbourg, 1 rue Blaise Pascal, BP 296 R8, 67008 Strasbourg, Cedex (France)

^d Université de Strasbourg, Institute for Advanced Study (USIAS), Strasbourg (France)

^e Institut des Sciences Moléculaires de Marseille, Aix Marseille Université, CNRS, Centrale Marseille, ISM2 UMR 7313, 13397, Marseille, France

E-mails: danopoulos@unistra.fr, braunstein@unistra.fr

Contents

Table S1. Crystal data and structure refinement for **3_{H-H}**, **3_{H-T}**, **8** and **9**.

Fig. S1 UV-visible-NIR absorption spectrum of **3_{H-T}** in CH₂Cl₂ ($c = 4.408 \cdot 10^{-5}$ mol L⁻¹).

Fig. S2 ¹H NMR signals (600 MHz, C₆D₆) of the ethylene ligands in complex **7**.

Fig. S3 UV-visible-NIR absorption spectrum of **8** in CH₂Cl₂ ($c = 8.074 \cdot 10^{-5}$ mol L⁻¹).

Fig. S4 ¹H NMR signals (400 MHz, C₆D₆) of the ethylene ligands in complex **9**.

Fig. S5 Cyclic voltammograms of **3_{H-T}** with added ferrocene (CH₂Cl₂ + 0.1 M [n-Bu₄N]PF₆, glassy carbon electrode, scan rate 0.1 Vs⁻¹, vs. Fc^{+/Fc}).

Fig. S6 Cyclic voltammograms of **8** with added ferrocene (CH₂Cl₂ + 0.1 M [n-Bu₄N]PF₆, glassy carbon electrode, scan rate 0.1 Vs⁻¹, vs. Fc^{+/Fc}).

Fig. S7 Cyclic voltammograms of **3_{H-H}** (top) and **3_{H-H}** with added ferrocene (bottom) (CH₂Cl₂ + 0.1 M [n-Bu₄N]PF₆, glassy carbon electrode, scan rate 0.1 Vs⁻¹, vs. Fc^{+/Fc}).

Fig. S8 A) Time-resolved UV-visible-NIR spectra of **3_{H-T}** for the first oxidation step (transition Ir(I)/Ir(I) to Ir(I)/Ir(II)) in CH₂Cl₂ + 0.1 M [n-Bu₄N]PF₆ (spectra recorded every 5 s). B) UV-visible spectral evolution for the first oxidation step.

Fig. S9 A) Time-resolved UV-visible-NIR spectra of **8** for the first oxidation step (transition Rh(I)/Rh(I) to Rh(I)/Rh(II)) in CH₂Cl₂ + 0.1 M [n-Bu₄N]PF₆ (spectra recorded every 5 s). B) Time-resolved UV-visible-NIR differential spectra for the first oxidation step.

Fig. S10 EPR spectra of the Rh(I)/Rh(II) system **8** electrochemically generated in CH₂Cl₂

at 100 K: a) Experimental spectrum b) Simulated spectrum with one ^{103}Rh nucleus (left) and two equivalent ^{103}Rh nuclei (right).

Fig. S11 Optimized structure of the Rh(I)/Rh(II) system with relevant interatomic distances.

Fig. S12 Spin population distribution (left) and Singly Occupied Molecular Orbital (SOMO) of the Rh(I)/Rh(II) system (right).

Fig. S13 Optimized structure of the Ir(I)/Ir(II) system with relevant interatomic distances.

Fig. S14 Spin population distribution (left) and Single Occupied Molecular Orbital (SOMO) of the Ir(I)/Ir(II) system (right).

Table S1. Crystal data and structure refinement for **3_{H-H}**, **3_{H-T}**, **8** and **9**.

	3_{H-H}	3_{H-T}	8	9
Empirical formula	C ₄₀ H ₅₀ Ir ₂ N ₄	C ₄₀ H ₅₀ Ir ₂ N ₄	C ₄₀ H ₅₀ Rh ₂ N ₄	C ₃₈ H ₅₄ N ₄ Rh ₂
Fw	971.24	971.24	792.66	772.67
T/K	173(2)	173(2)	173(2)	173(2)
Crystal system	Triclinic	Monoclinic	Monoclinic	Triclinic
Space group	<i>P</i> -1	<i>P</i> 2 ₁ /c	<i>P</i> 2 ₁ /c	<i>P</i> -1
<i>a</i> /Å	10.533(3)	12.3621(4)	12.4452(7)	8.5688(17)
<i>b</i> /Å	12.162(3)	18.9590(6)	18.7469(10)	14.354(3)
<i>c</i> /Å	14.504(4)	17.3685(5)	17.5877(7)	16.312(3)
α /°	86.570(6)	90	90	93.13(3)
β /°	85.210(6)	119.356(2)	119.594(3)	91.35(3)
γ /°	69.345(6)	90	90	95.87(3)
<i>V</i> /Å ³	1731.5(7)	3547.99(19)	3568.1(3)	1991.9(7)
<i>Z</i>	2	4	4	2
μ /mm ⁻¹	7.712	7.528	0.958	0.856
No. of rflns collected	35403	37595	32340	20590
No. unique rflns	10116	12351	10482	9057
R(int)	0.0643	0.0273	0.0358	0.0519
Goodness of fit on <i>F</i> ²	1.137	1.111	1.025	1.012
Final <i>R</i> indices [<i>I</i> >2σ(<i>I</i>)]	R1 = 0.0855 wR2 = 0.2408	R1 = 0.0332 wR2 = 0.0580	R1 = 0.0347 wR2 = 0.0695	R1 = 0.0363 wR2 = 0.1021
<i>R</i> indices (all data)	R1 = 0.1050 wR2 = 0.2547	R1 = 0.0561 wR2 = 0.0674	R1 = 0.0671 wR2 = 0.0815	R1 = 0.0413 wR2 = 0.1062

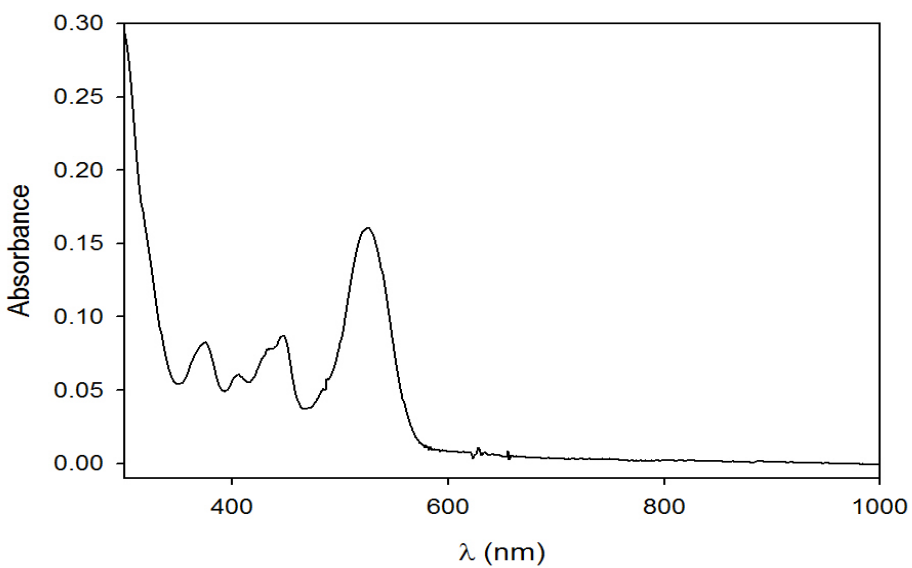


Fig S1 UV-visible-NIR absorption spectrum of **3_{H-T}** in CH₂Cl₂ ($c = 4.408 \times 10^{-5}$ mol L⁻¹).

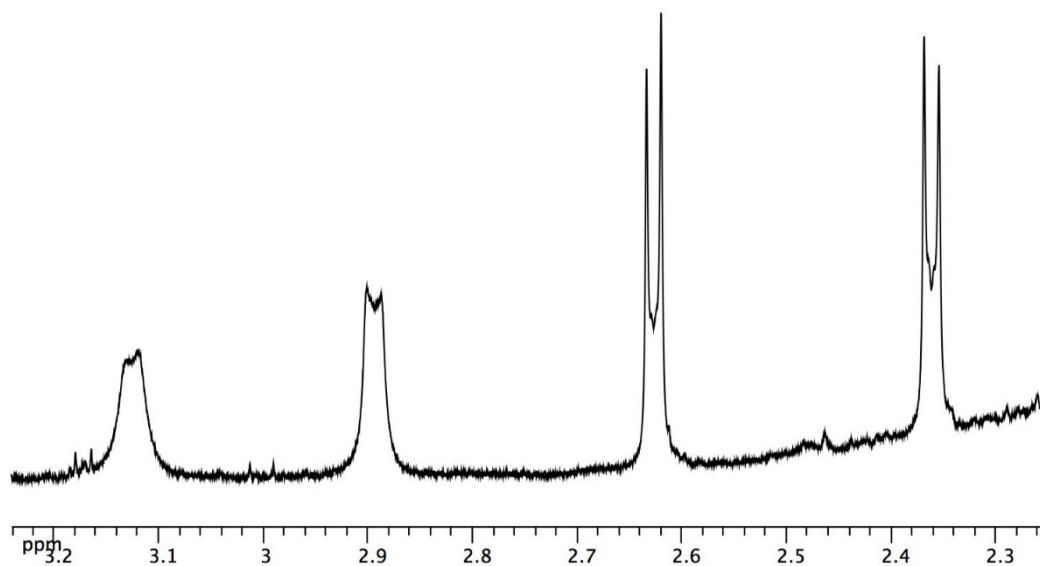


Fig. S2 ¹H NMR signals (600 MHz, C₆D₆) of the ethylene ligands in complex **7**.

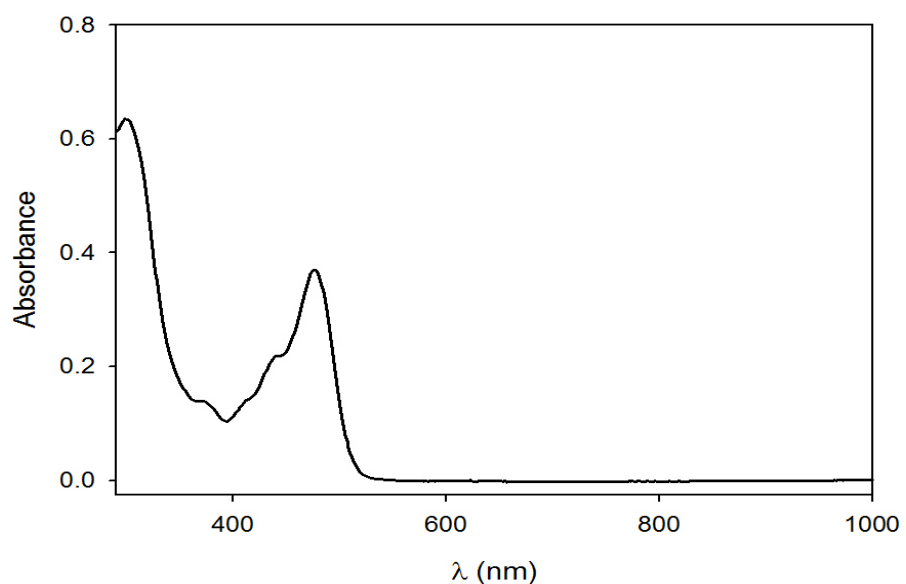


Fig. S3 UV-visible-NIR absorption spectrum of **8** in CH_2Cl_2 ($c = 8.074 \times 10^{-5} \text{ mol L}^{-1}$).

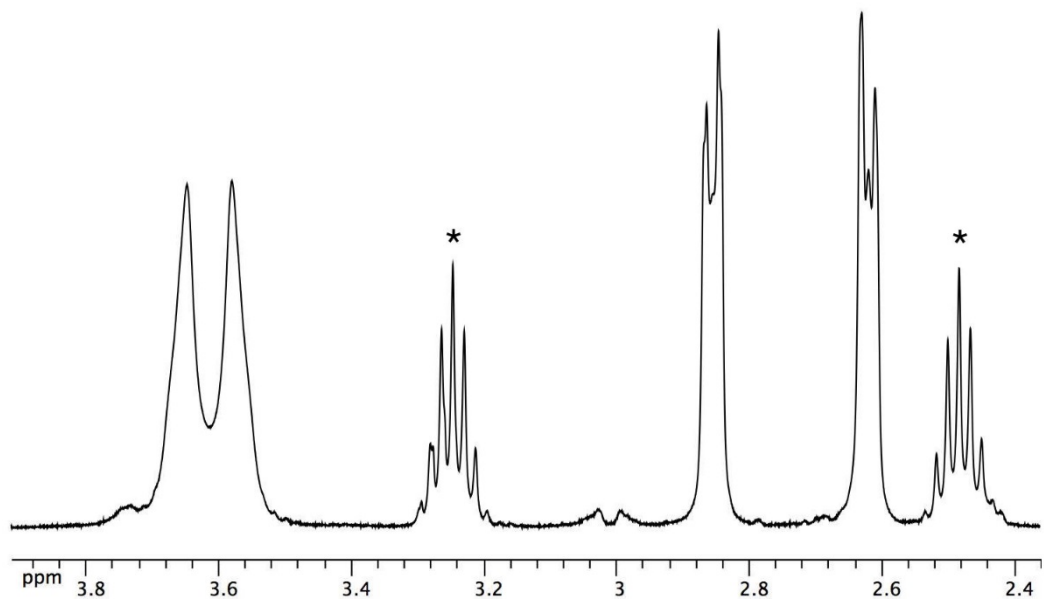


Fig. S4 ^1H NMR signals (400 MHz, C_6D_6) of the ethylene ligands in complex **9**. (*) for $\text{CH}(\text{CH}_3)_2$ of Dipp)

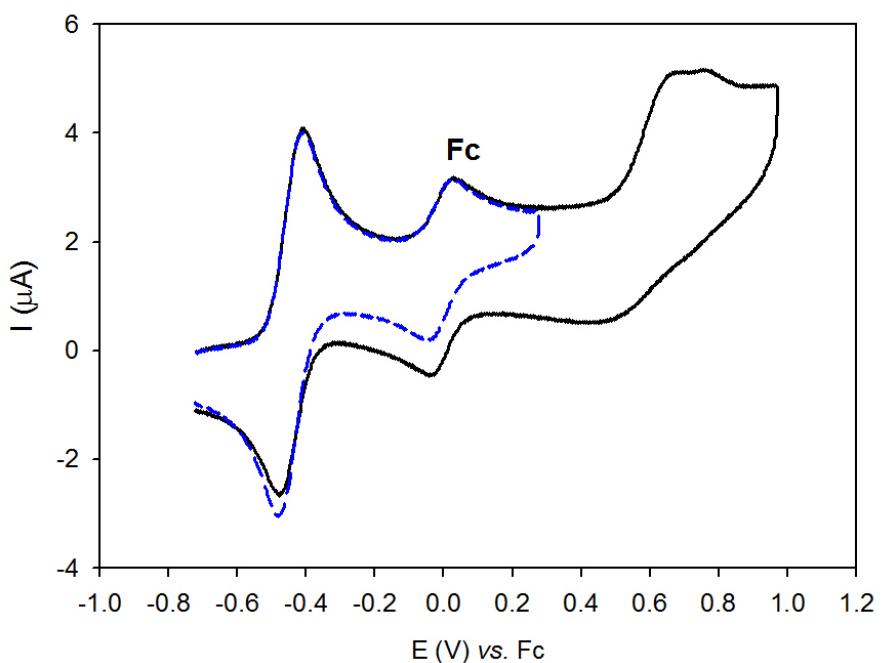


Fig. S5 Cyclic voltammograms of **3_{H-T}** with added ferrocene ($\text{CH}_2\text{Cl}_2 + 0.1 \text{ M } [n\text{-Bu}_4\text{N}]PF_6$, glassy carbon electrode, scan rate 0.1 Vs^{-1} , vs. Fc^+/Fc).

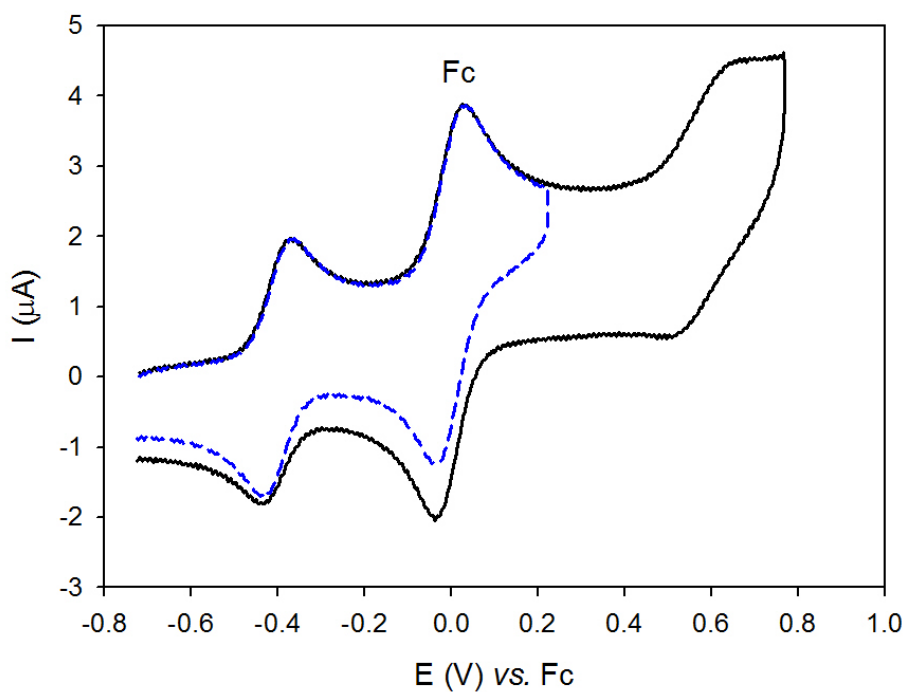


Fig. S6 Cyclic voltammograms of **8** with added ferrocene ($\text{CH}_2\text{Cl}_2 + 0.1 \text{ M } [n\text{-Bu}_4\text{N}]PF_6$, glassy carbon electrode, scan rate 0.1 Vs^{-1} , vs. Fc^+/Fc).

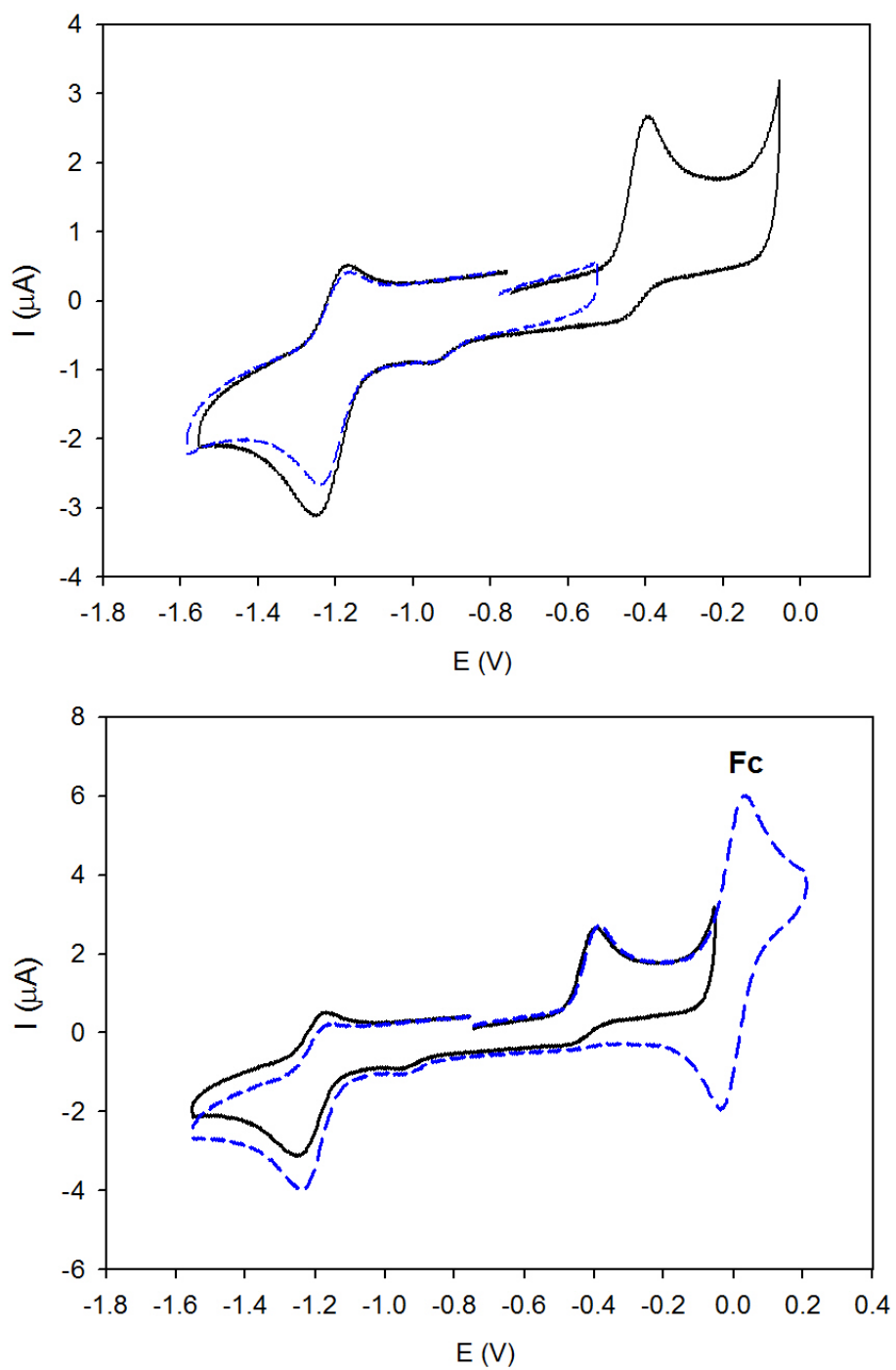


Fig. S7 Cyclic voltammograms of $\mathbf{3}_{\text{H-H}}$ (top) and $\mathbf{3}_{\text{H-H}}$ with added ferrocene (bottom) ($\text{CH}_2\text{Cl}_2 + 0.1 \text{ M} [n\text{-Bu}_4\text{N}] \text{PF}_6$, glassy carbon electrode, scan rate 0.1 Vs^{-1} , vs. Fc^+/Fc).

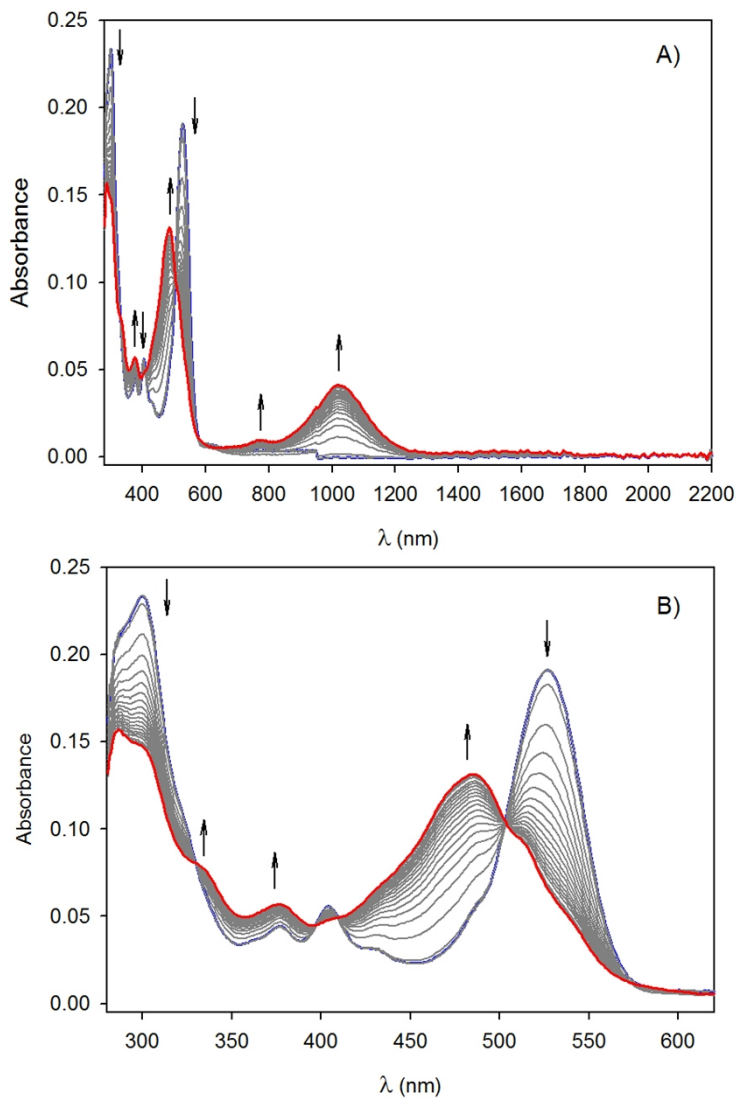


Fig. S8 A) Time-resolved UV-visible-NIR spectra of **3_{H-T}** for the first oxidation step (transition Ir(I)/Ir(I) to Ir(I)/Ir(II)) in CH₂Cl₂ + 0.1 M [n-Bu₄N]PF₆ (spectra recorded every 5 s). B) UV-visible spectral evolution for the first oxidation step.

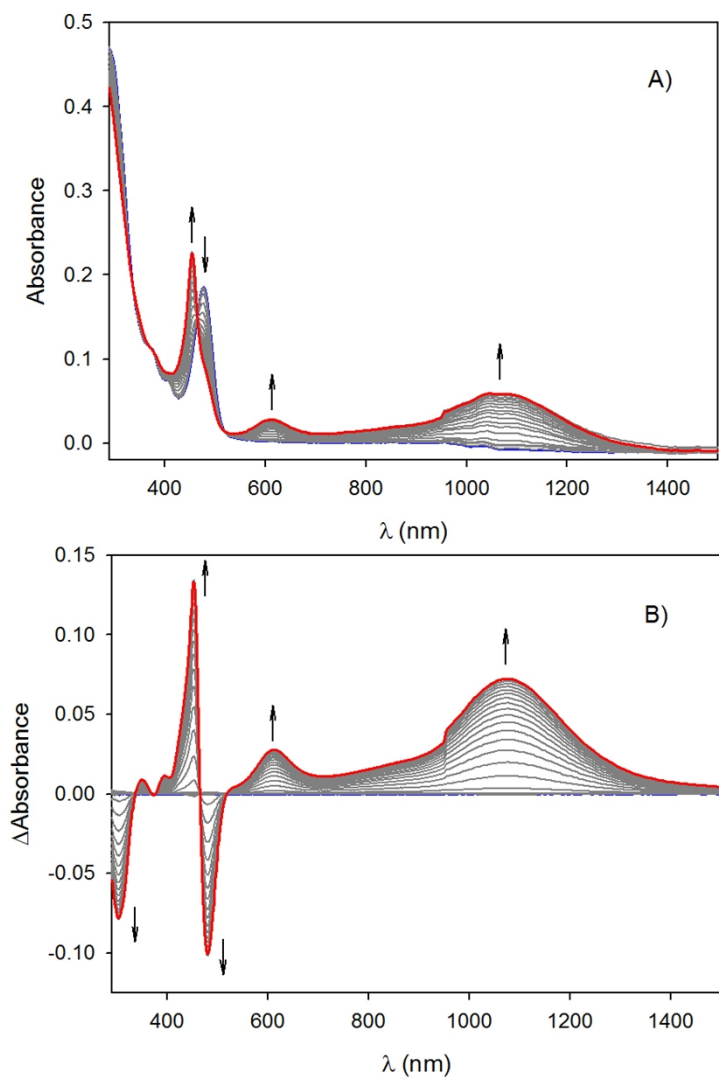


Fig. S9 A) Time-resolved UV-visible-NIR spectra of **8** for the first oxidation step (transition Rh(I)/Rh(I) to Rh(I)/Rh(II)) in $\text{CH}_2\text{Cl}_2 + 0.1 \text{ M} [n\text{-Bu}_4\text{N}] \text{PF}_6$ (spectra recorded every 5 s). B) Time-resolved UV-visible-NIR differential spectra for the first oxidation step.

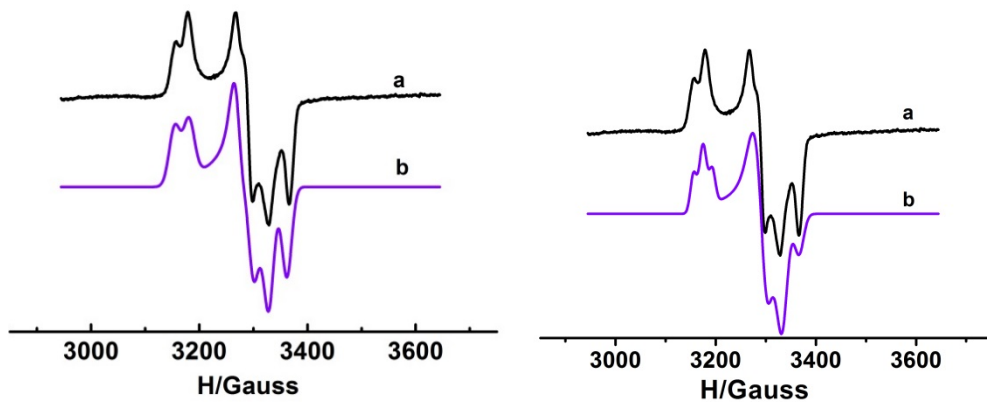


Fig. S10 EPR spectra of the Rh(I)/Rh(II) system **8** electrochemically generated in CH_2Cl_2 at 100 K: a) Experimental spectrum b) Simulated spectrum with one ^{103}Rh nucleus (left) and two equivalent ^{103}Rh nuclei (right).

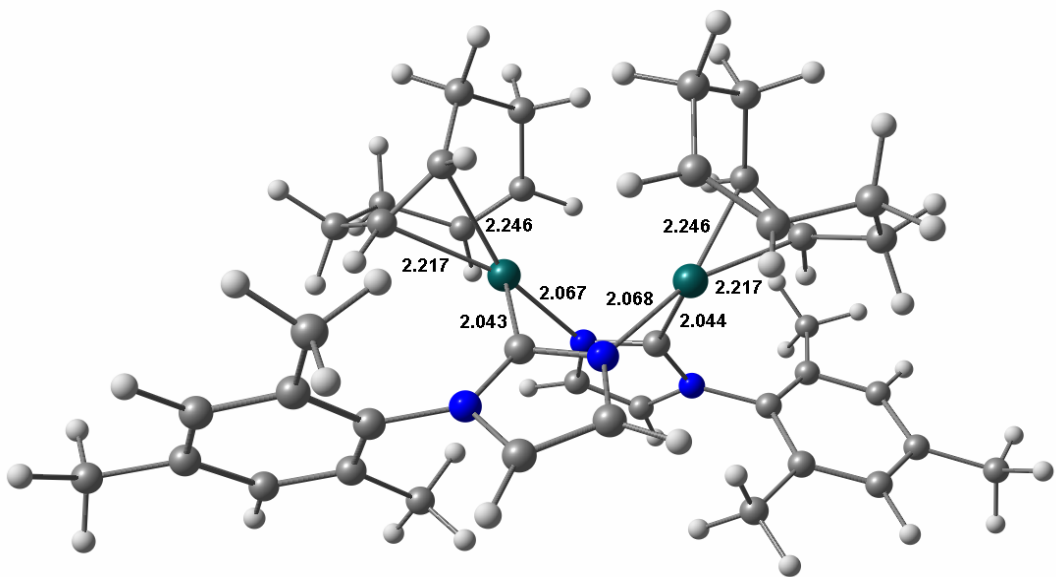


Fig. S11 Optimized structure of the Rh(I)/Rh(II) system with relevant interatomic distances.

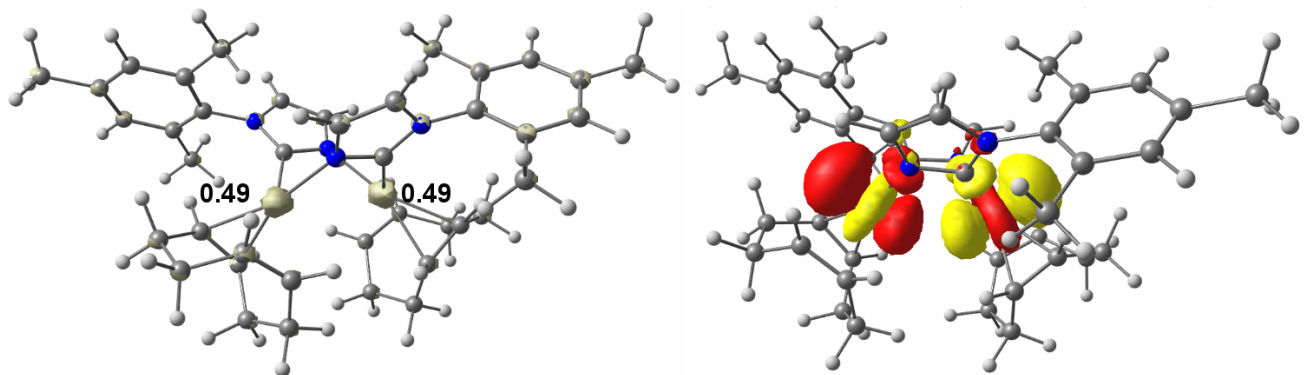


Fig. S12 Spin population distribution (left) and Singly Occupied Molecular Orbital (SOMO) of the Rh(I)/Rh(II) system (right).

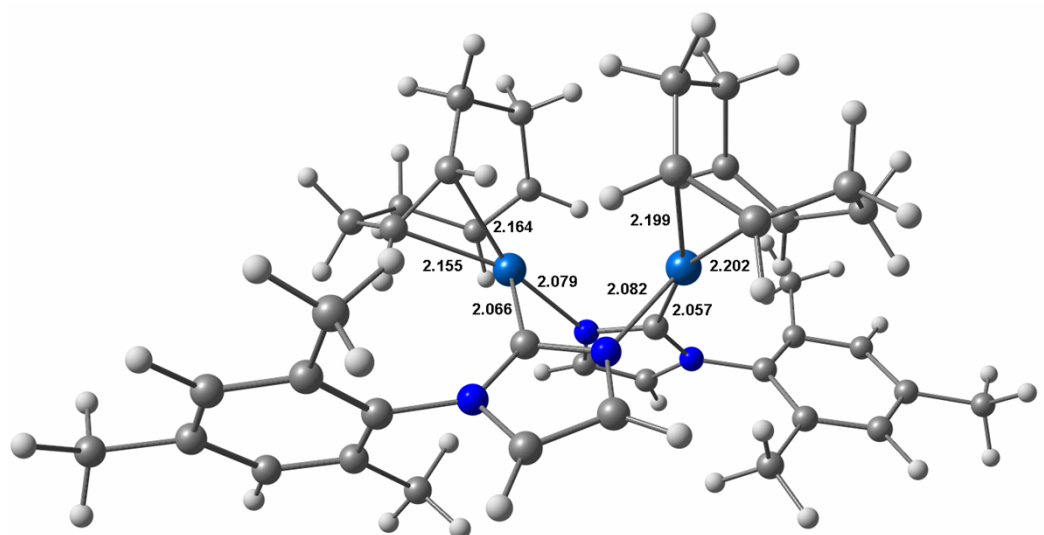


Fig. S13 Optimized structure of the Ir(I)/Ir(II) system with relevant interatomic distances.

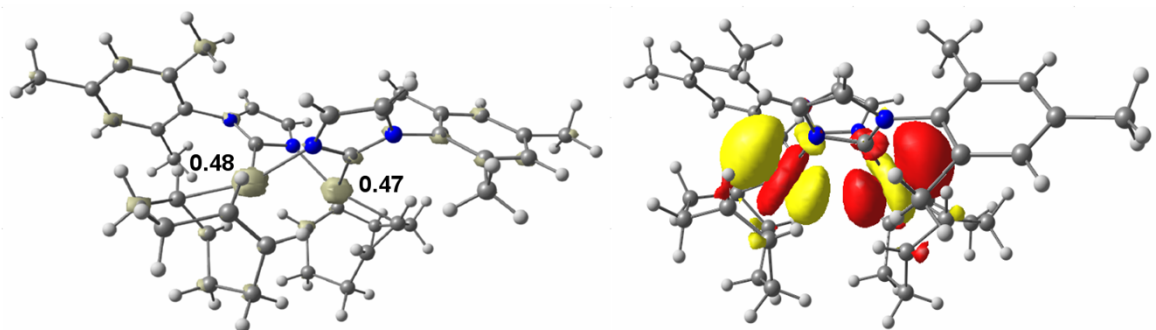


Fig. S14 Spin population distribution (left) and Singly Occupied Molecular Orbital (SOMO) of the Ir(I)/Ir(II) system (right).